Korean J. Chem. Eng., 35(12), 2384-2393 (2018)
DOI: 10.1007/s11814-018-0181-y

pISSN: 0256-1115
eISSN: 1975-7220

Hydrogels with diffusion-facilitated porous network for improved adsorption performance

Yan-yan Pei‡, Dong-mei Guo‡, Qing-da An†, Zuo-yi Xiao, Shang-ru Zhai†, and Bin Zhai

Faculty of Light Industry and Chemical Engineering, Dalian Polytechnic University, Dalian 116034, China
(*Received 4 May 2018 • accepted 25 October 2018*)

Abstract−Porous alginate-based hydrogel beads (porous ABH) have been prepared through a facile and sustainable template-assisted method using nano-calcium carbonate and nano-$CaCO_3$ as pore-directing agent for the efficient capture of methylene blue (MB). The materials were characterized by various techniques. The sorption capacities of ABH towards MB were compared with pure sodium alginate (ABH-1:0) in batch and fixed-bed column adsorption studies. The obtained adsorbent (ABH-1:3) has a higher BET surface area and a smaller average pore diameter. The maximum adsorption capacity of ABH-1:3 obtained from Langmuir model was as high as 1,426.0 mg g^{-1}. The kinetics strictly followed pseudo-second order rate equation and the adsorption reaction was effectively facilitated, approximately 50 minutes to achieve adsorption equilibrium, which was significantly shorter than that of ABH-1:0. The thermodynamic parameters revealed that the adsorption was spontaneous and exothermic. Thomas model fitted well with the breakthrough curves and could describe the dynamic behavior of the column. More significantly, the uptake capacity of ABH-1:3 was still higher than 75% of the maximum adsorption capacity even after ten cycles, indicating that this novel adsorbent can be a promising adsorptive material for removal of MB from aqueous solution under batch and continuous systems.

Keywords: Porous Structures, Hydrogel Beads, Nano-$CaCO_3$, Dye, Adsorption

INTRODUCTION

Methylene blue (MB), as a very common cationic organic dye, has been extensively used in many industrial fields such as leather, textile, food, pulp and paper. However, MB has high toxicity and potentially carcinogenic effect on human health, which can lead to severely damage the eyes, skin, and respiratory and digestive system [1,2]. Therefore, removing MB-containing wastewater to an acceptable level prior to discharging into the natural system is critical [3]. Currently, a number of promising technologies have been applied for removal of dye, including adsorption [4,5], membrane filtration [6], photo-catalytic degradation [7], and biological treatments [8]. Among them, adsorption appears to be a simple and attractive approach owing to its low cost, high treatment efficiency and simple operation [9,10]. Meanwhile, all kinds of adsorbents have been explored for MB removal from wastewater, such as activated carbon [11], montmorillonite (MMT) clays [12], bio-sorbents [13,14], and magnetic porous carbon microspheres (MPCMs) [15]. However, searching for a cost-effective, environmentally friendly and easily available sorption media for MB removal from wastewater still remains a vital issue.

Recently, some natural bio-sorbents, such as chitosan, sodium alginate (SA) and cellulose, have been attractive owing to their being low cost, easily available, non-toxic, biodegradable and renewable. In addition, there are many functional groups on the chains of these materials which can be modified through various methods to improve their adsorption capacity [16-18]. Among them, SA, a natural biopolymer extracted mainly from brown seaweed, is composed of β-D-mannuronic (M units) and α-L-guluronic acid (G units), and it can be transformed into hydrogels through chelating with multivalent metal ions [19]. In particular, SA has abundant carboxyl and hydroxyl groups per unit which are excellent functional platforms to remove cationic pollutant such as MB from aqueous solution through physical and chemical modifications. SA hydrogels have good sorption capacity for the removal of dye from effluents on a practical scale [20-22]. However, the previously reported adsorption performance of alginate-based nanocomposite materials is not fully explored and applied. For example, Hassan et al. reported the adsorption capacity of MB on AB hydrogels was only 800 mg g^{-1} [23]. Mohammed et al. reported that cellulose nanocrystals and alginate (CNC-ALG) hydrogel beads have a maximum adsorption capacity of 256.41 mg g^{-1} [24]. Noticeably, both the adsorption capacity and sorption kinetics are not parallel to those practical processes that require diffusion-facilitated pathways and accessible adsorption sites.

Accordingly, there is an urgent need to prepare porous hydrogels with controlled porosity and high specific surface area for rapid diffusion of dye molecules into network and interacting with its functional groups for the efficient adsorption of MB. Even though SA hydrogels beads have porous structures, there are other controllable ways to further increase their porosity to enlarge the pore size and specific surface area, which possibly enhance the adsorption capacity [25]. Two effective methods can be employed to enhance the adsorption performance of porous hydrogel beads, including freeze-drying and adding nano-$CaCO_3$. The added nano-$CaCO_3$

†To whom correspondence should be addressed.
E-mail: anqingdachem@163.com, zhaisrchem@163.com
‡These two authors contributed equally to this paper.

can serve as pore-forming agent in the interior structure of SA which is then washed with diluted hydrochloric acid generating void holes at the sites which were occupied by solid particles previously. The freeze-drying can exhibit relatively more porosity and improve the maximum adsorption capacities of the material [26]. Compared with the previous study, the two approaches mentioned above were found to be more efficient, easy to synthesize, and easier for large-scale application. Thus, it is of great interest to develop template-assisted method to prepare hydrogel beads with high surface area and mechanically stable porous framework.

Herein, a new type of low-cost and eco-friendly ABH-1:3 with high-surface-area and small-pore-diameter was fabricated for the rapid removal of MB. The effect of the different mass ratios of SA, $CaCl_2$ and nano-$CaCO_3$ on the properties of porous beads was investigated. Subsequently, the removal of MB on ABH was investigated systematically through batch and fixed-bed column adsorption to evaluate its adsorption performance. In batch study, the adsorption kinetics, isotherms, thermodynamics and the effect of pH were investigated to evaluate the fundamental adsorption process and performance of the ABH. In a fixed-bed column study, the effects of initial concentration and flow rate were also discussed in detail. In addition, the recyclability of the ABH-1:3 was examined using 0.1 M HCl/ethanol as an eluent. N_2 adsorption/desorption techniques, Fourier transform infrared spectroscopy (FTIR), scanning electron microscopy (SEM), and X-ray powder diffraction (XRD) were utilized to characterize the pore structure of ABH.

MATERIAL AND METHODS

1. Materials

Sodium alginate with a high viscosity (14,000 cP of 2% solution) and MB were supplied from Sinopharm Chemical Reagent Corporation, China. Calcium chloride anhydrous ($CaCl_2$), ethanol, hydrochloric acid (HCl) and sodium hydroxide (NaOH) were obtained from Tianjin Kermel Chemical Reagent Factory, China. Nano-$CaCO_3$ (800 nm) was provided by Sigma-Aldrich Co., Ltd. All chemicals were of analytical grade and used as received without any further purification. Deionized water was used for the preparation of all the required solutions. MB stock solution (1.0 g L^{-1}) was prepared by dissolving MB in deionized water.

2. Synthesis of ABH Hydrogel Beads

About 4 g SA and a certain amount of nano-$CaCO_3$ powder (0, 1.0, 2.0, 3.0, 4.0 and 6.0 g) were introduced into 200 mL deionized water and continuously stirred until a homogeneous suspension was formed. The suspension was then dropwise added into cross-linking solution (5 wt% $CaCl_2$) by using a peristaltic pump (LEAD-FLUID-Y215, China) with a flow rate of 3 mL min^{-1} to form uniform immobilized ABH beads (3-5 mm in diameter each). Then, the beads were left for 24 h to complete solidification. After 24 h immersion, the beads were taken out and subsequently washed by HCl aqueous solution (1 mol L^{-1}) under slow shaking (25 rpm) for another 1.5 h to remove $CaCO_3$ producing internal porosity. The hydrogel beads were then filtered and washed with plenty of deionized water to remove residual H^+, Cl^- and Ca^{2+} ions, and freeze-dried (−50 °C, 0.1 mbar) for 48 h under vacuum (less than 10 Pa).

Sorbents with different amounts of SA (1%, 2%, 3% w/v) and constant $CaCl_2$ (5 % w/v) were prepared. Then sorbents with different amounts of $CaCl_2$ (1%, 3%, 5%, 7%, 9% w/v) and constant SA (2% w/v) were also prepared. The corresponding results are demonstrated in Fig. S1 and Table S1. Fig. S1 and Table S1 show that the maximum adsorption capacity of MB was SA (2% w/v) and $CaCl_2$ (5% w/v). To further investigate the effect of nano-$CaCO_3$ content on MB, ABH with SA/nano-$CaCO_3$ content (1 : 0, 1 : 1, 1 : 2 and 1 : 3) and constant mixing mass ratio of $CaCl_2$ (5% w/v) to SA (2% w/v) were prepared (abbreviated as ABH-1:0) (Fig. S1, Table S1). Similarly, ABH-1:0, ABH-1:1, ABH-1:2 and ABH-1:3 hydrogel beads were prepared according to the same procedure. The fabrication process of ABH-1:3 is depicted in Scheme 1.

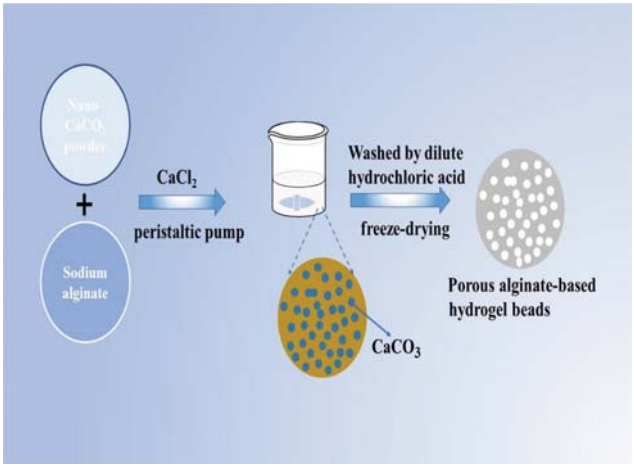

Scheme 1. Schematic illustration of synthesis of porous alginate-based hydrogel beads.

3. Characterization

The morphology and microstructure of as-prepared ABH hydrogel beads was obtained by scanning electron microscopy (SEM, JSM-6460LV, JEOL, Japan). The specific surface area and pore diameter of the samples were performed by nitrogen adsorption-desorption experiments at 77.3 K (Quantachrome AutosorbNOVA2200e, USA) after the samples were degassed in the flow of N_2 at 110 °C overnight. The phase structures were observed using X-ray diffraction (XRD, Shimadzu XRD-6100 diffractometer) at 40 kV and 40 mA for Cu Kα radiation (λ=1.5406 Å) from 10 to 80° at a scan rate of 8° min^{-1}. Fourier Transform infrared spectra (FTIR, Perkin-Elmer, USA) at a resolution of 4 cm^{-1} in the wavenumber range of 4,000-400 cm^{-1} were acquired using KBr pellets to identify the functional groups of the synthesized sorbents. The pH was determined using a pH meter (pHS-2F, LEICI Instruments, China), and the pH values of MB solution were adjusted by adding 0.1 M solution of HCl or NaOH.

4. Batch Adsorption Studies

Batch experiments were conducted to evaluate the adsorption performance of ABH-1:3 towards MB. To optimize MB removal conditions, a series of parameters including the effects of pH (2.0-12.0), contact time (0-24 h), initial MB concentration (30-800 mg L^{-1}) and temperature (298-318 K) were investigated. For batch adsorption experiments, about 10 mg of ABH-1:3 adsorbent was added to the 50 mL conical flask containing 20 mL MB solution of desired

concentrations (30-800 mg L^{-1}) for a certain time at 298 K. Subsequently, the adsorbent was separated by a 4.5 μm pore size membranes and the residual concentrations in the solution was immediately determined by a double beam UV-Vis spectrophotometer (UV-1600PC, Shanghai Mapada Instruments, China) at the wavelength of 664 nm.

All of these adsorption experiments were repeated three times, using average values as the results, and the standard deviations of three times experiments were denoted by error bars. The equilibrium adsorption capacity (Q_t, mg g^{-1}) and the removal efficiency (R%) were calculated using the following equations [27,28]:

$$Q_t = \frac{(C_0 - C_t)V}{M} \quad (1)$$

$$R\% = \frac{C_0 - C_t}{C_0} \times 100\% \quad (2)$$

where Q_t (mg g^{-1}) is the equilibrium adsorption capacity, C_0 and C_t (mg L^{-1}) are the concentrations of MB at initial and time t, respectively. V (L) and M (g) are the volume of MB solution and the adsorbent dosage, respectively.

5. Column Adsorption Studies

Fixed-bed column adsorption experiments were carried out using a glass column (0.8 cm inner diameter ×12 cm) in which the adsorbents (0.035 g) were added from the top of the column and the final bed depth was 10 cm. Glass wool was placed at both ends of the column to avoid the hydrogel beads leaving the column. The MB solution with predetermined initial concentrations (50, 100, and 200 mg L^{-1}) was pumped upwards through the glass column using a peristaltic pump at a desired flow rate. The effluent solution was collected in regular time intervals and then measured using an UV-Vis spectroscopy. Breakthrough curves were obtained by plotting C_t/C_0 against t. Column mode parameters were calculated according to previous reported studies [21,29]. All the experiments were at room temperature (298±2 K).

The treated effluent volume V_t (mL) can be calculated using the following equation:

$$V_t = Qt_e \quad (3)$$

The maximum column adsorption capacity q_{total} (mg) was calculated as follows:

$$q_{total} = \int_0^{V_t} (C_0 - C_t)dV \quad (4)$$

where C_0 (mg L^{-1}), C_t (mg L^{-1}), Q (mL min^{-1}) and t (min) are the influent MB concentration, the effluent MB concentration, volumetric flow rate and the total flow time, respectively.

The amount of MB adsorbed at equilibrium in the column was evaluated according to the following equation:

$$q_m = \frac{q_{total}}{m} \quad (5)$$

where m (g) is the mass of adsorbent in the column.

RESULTS AND DISCUSSION

1. Texture and Surface Characterization of the Materials

The XRD patterns of nano-$CaCO_3$ powder and ABH-1:3 are presented in Fig. S2. Nano-$CaCO_3$ has characteristic diffraction peaks at 2θ of 23.0° (012), 29.4° (104), 31.5° (006), 36.0° (110), 39.5° (113), 43.2° (202), 47.5° (018), 48.5° (116) and 57.6° (122), corresponding to calcite phase of $CaCO_3$ (JCPDS no. 005-0586), respectively [30]. Meanwhile, the ABH-1:3 has two broad diffraction peaks on the X-ray diffraction pattern, including the peak at 2θ of 22.5° and the low-angle peak at 2θ of 13.4°, which could be attributed to the shell structure of alginate [31]. In addition, all characteristic peaks of $CaCO_3$ disappear in the XRD pattern of ABH-1:3, indicating that $CaCO_3$ had been completely removed from the hydrogel beads by

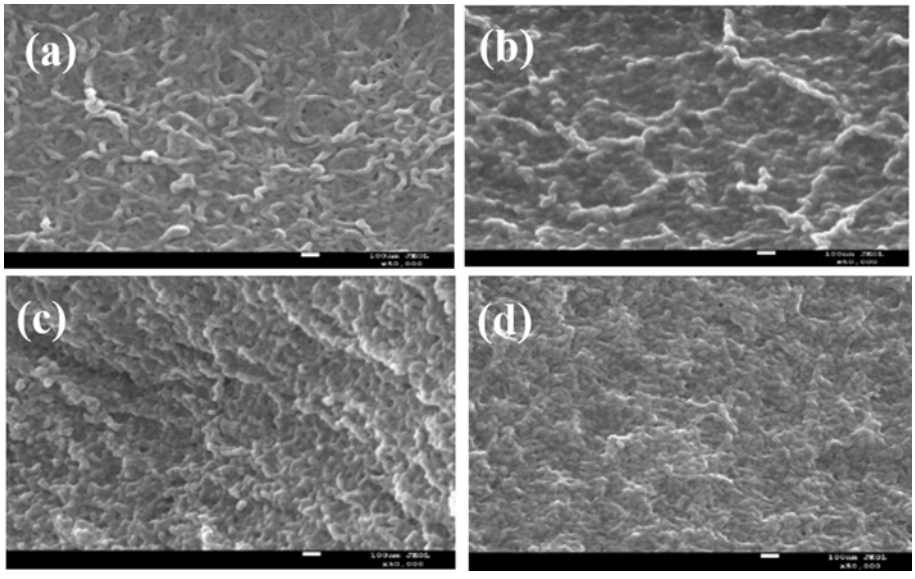

Fig. 1. The surface morphologies of SEM images of ABH with different nano-$CaCO_3$ contents (a) ABH-1:0, (b) ABH-1:1, (c) ABH-1:2 and (d) porous ABH-1:3.

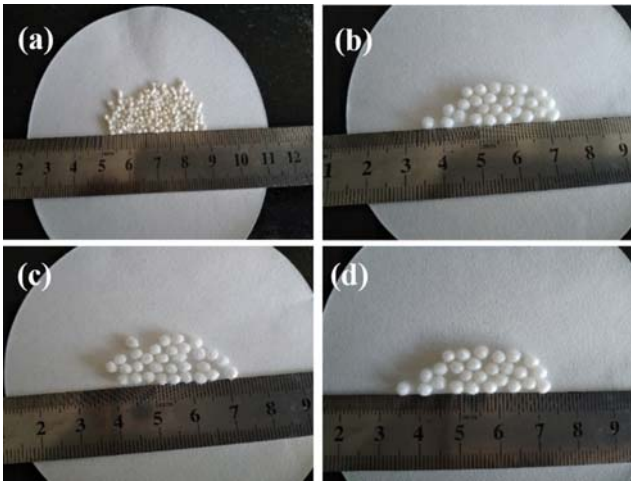

Fig. 2. The photos of ABH-1:0, ABH-1:1, ABH-1:2 and ABH-1:3.

a simple acid treatment.

The surface morphologies and microstructures of ABH-1:0, ABH-1:1, ABH-1:2 and porous ABH-1:3 were characterized by SEM, and the results are in Fig. 1. As shown, hydrogel beads have an interconnected porous structure which contains abundant pores with the width of numerous nanometers and the pores become slightly smaller with increasing the nano-$CaCO_3$ in ABH from 1 : 1 to 1 : 3 (Fig. 1(b), (c), (d)). As shown in the photos of Fig. 2, all the particles are spherical with a remarkably similar size of 3-5 mm except ABH-1:0 whose particle size is in the range of 2-3 mm after freeze-drying. This may be attributed to the fact that addition of $CaCO_3$ could diminish the possibility of the collapse of hole after freeze-drying, which could significantly improve the specific surface area of adsorbent and further enhance the adsorption performance of porous hydrogel beads.

Fig. 3 shows the N_2 adsorption desorption isotherms and the pore size distribution curves of four adsorbents. The observed isotherms (Fig. 3(a)) of four adsorbents correspond to the typical type-IV isotherm, which is a typical characteristic of mesoporous materials. Compared with other adsorbents, ABH-1:0 exhibits an H_2-type hysteresis loop, whereas ABH-1:1, ABH-1:2 and ABH-1:3 are H_4-type hysteresis loop in the relative pressure (P/P_0) range of 0.3-1.0. In addition, typical capillary condensation was observed within the relative pressure range of 0.4-0.95 for ABH-1:1, ABH-1:2 and ABH-1:3. According to the BJH pore size distribution (Fig. 3(b)), it was observed that the porous ABH pore size is less than 5 nm, indicating that ABH has relatively uniform mesoporous structure [32]. Note that the mesoporous structure is advantageous for mass transfer between the solid phases and the aqueous. Thus, the porous ABH-1:3 (2.01 nm) might facilitate the adsorption of MB molecules, considering that the molecular size of MB is only 1.382 nm [33]. The textural properties of all prepared adsorbents are summarized in Table S2. It was observed that, the BET surface area of the four samples was 21.8, 57.5, 73.0 and 91.9 $m^2 g^{-1}$, respectively, which might be attributed to the gradual decrease in pore size. With the increase of the proportion of $CaCO_3$, the samples surface area also increased, which is favorable for promoting its adsorption performance [34]. Moreover, the total pore volume and average pore diameter decreased gradually from 0.116 to 0.043 $cm^3 g^{-1}$ and from 5.79 to 3.449 nm, respectively, suggesting that more mesoporous structures were present with the removal of nano-$CaCO_3$. The increase in proportion of nano-$CaCO_3$ during the synthesis process is favorable for the formation of the developed porous framework.

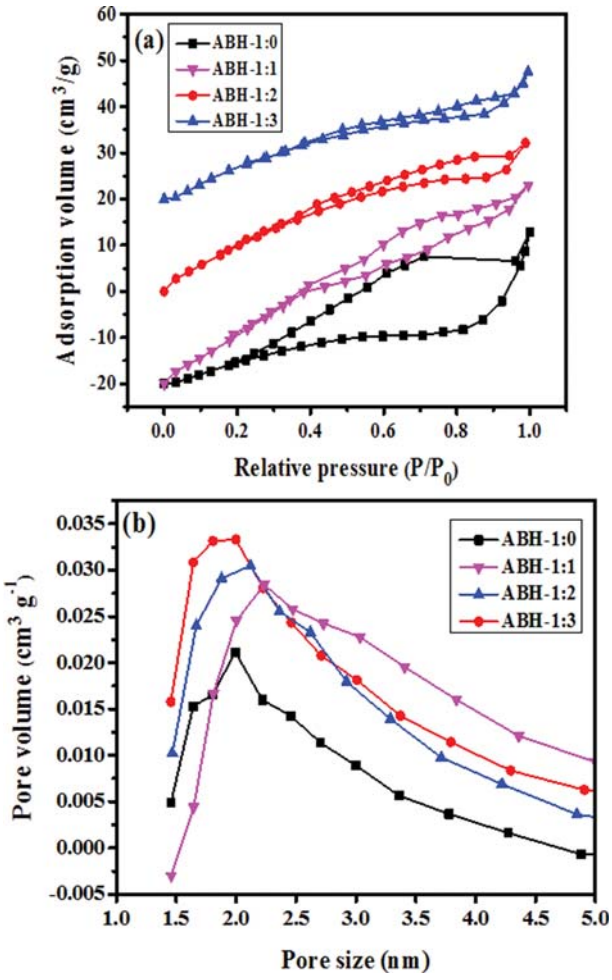

Fig. 3. N_2 adsorption and desorption isotherms (a) and BJH pore size distributions (b) of ABH-1:0, ABH-1:1, ABH-1:2 and ABH-1:3.

The FT-IR spectra of the $CaCO_3$, ABH-1:0 ABH-1:3 and ABH-1:0-MB are shown in Fig. S3. The strong peaks of all the samples at 3,435 cm^{-1} correspond to the -OH stretching vibrations. The peak at 2,926 cm^{-1} relates to the axial stretching vibrations of aliphatic C-H, and the weak peak at 1,079 cm^{-1} originates from -C-O stretching vibration which is similar to that of previous studies [35]. The peaks located at 1,623 cm^{-1} of all the samples can be attributed to the presence of COO^- groups in alginate [36]. From the comparison of ABH-1:3 and $CaCO_3$, the peaks at 2,513 cm^{-1} and 1,796 cm^{-1} disappeared, indicating that $CaCO_3$ was removed from hydrogels, which is consistent with the XRD results (Fig. S2). By comparing the result of ABH-1:3 before and after MB sorption, it can be seen that many functional groups transferred or appeared. For example, the peak located at 1,079 cm^{-1} was increased to 1,135 cm^{-1}. In contrast, the peaks at 1,337 and 885.5 cm^{-1} appeared after adsorption. It clearly proves that the adsorption process had taken place between

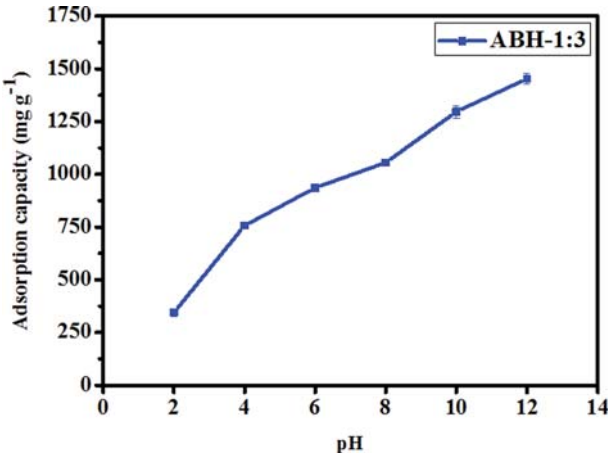

Fig. 4. Effect of the pH on the MB adsorption onto ABH-1:3 (adsorbent dose, 10 mg; volume, 20 mL; initial concentration of MB, 700 mg L^{-1}; contact time, 24 h and temperature, 298±2 K).

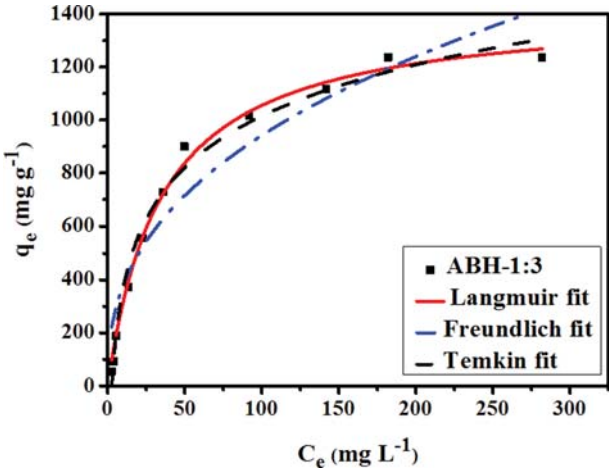

Fig. 5. The adsorption isotherms of the Langmuir, Freundlich and Temkin (initial concentration, 30-800 mg L^{-1}; contact time, 24 h; adsorbent dose, 10 mg and MB solution, 20 mL).

dye molecules and porous alginate beads [22].

2. Effect of pH on MB Adsorption

The pH of solution played a vital role in affecting the adsorption process of the pollutants, especially for the adsorption capacity. The effect of solution pH on the adsorption of dye over the ABH-1:3 was investigated at a pH range of 2-12, and the results are shown in Fig. 4. The lowest adsorption capacity of MB was achieved when the pH value was 2. The adsorption capacity of MB on ABH-1:3 increased from 936.2 mg g^{-1} to 1,453.1 mg g^{-1} under the pH range of 6-12. At low pH, there is intense competition for available adsorption sites between the positive cationic dye molecules and the H^+ ions of the solution, leading to the decreased adsorption capacity. By contrast, higher adsorption capacity at a higher pH was attributed to the stronger electrostatic interaction between the adsorbent and cationic MB molecules. These results indicated that the adsorption capacity for MB under basic conditions was found to be higher than that of acidic conditions. Similar results have been reported in the previous literature [23,37,38].

3. Adsorption Isotherms

The equilibrium adsorption isotherm plays an important role in revealing the adsorption mechanism and surface properties. Moreover, the adsorption isotherm helps to describe the interactive behavior between adsorbed MB and residual dye in aqueous solution at adsorption equilibrium state. In this study, Langmuir isotherm, Freundlich isotherm and Temkin isotherm models were applied to fit the experimental data [39,40]. The equations can be written as:

$$q_e = \frac{q_m K_L C_e}{1 + K_L C_e} \quad (6)$$

$$R_L = \frac{1}{1 + K_L C_0} \quad (7)$$

$$q_e = K_F C_e^{1/n} \quad (8)$$

$$q_e = B \ln(AC_e) \quad (9)$$

where q_e (mg g^{-1}) is the adsorption capacity of MB on the adsorbent at equilibrium, and q_m (mg g^{-1}) is the maximum adsorption capacity under ideal conditions. C_0 (mg L^{-1}) and C_e (mg L^{-1}) are the concentrations of MB at initial and equilibrium state, respectively. K_L (m^3 g^{-1}) and K_F (mg g^{-1}) are the isotherm constants of Langmuir and Freundlich. n is the intensity of adsorption. A (L mg^{-1}) and B (mg g^{-1}) are Temkin isotherm constants.

The values of different parameters such as q_m, K_L, n, K_F, A and B could be obtained from the slope and intercept of the plots, which are shown in Fig. 5, and the results are presented in Table S3. As shown by the correction coefficient R^2, the Langmuir isotherm

Table 1. Comparison of maximum adsorption capacity of various adsorbents for the removal of dye

Adsorbent	Q_{max} (mg g^{-1})	Reference
Porous alginate-based hydrogel beads	1320.9	This study
Activated carbon-bentonite-alginate beads	757.0	22
Cellulose nanocrystals and alginate hydrogel beads	256.4	24
Sodium alginate (SA) beads	572	37
Epichlorohydrin-reticulated magnetic alginate beads	261.7	41
Alginate-halloysite nanotube hybrid bead	250	42
Activated organo-bentonite (AOBent)/sodium alginate (SA) composite beads	414	43
Alginate graft-polyacrylonitrile beads	3.51	44

(0.993) proved more suitable than the other two adsorption isotherms, implying the adsorption process belongs to monolayer adsorption with active sites homogeneously distribution over the adsorbent surface and no interaction between the adsorbed adsorbate molecules. The high q_m value of 1,426.0 mg g^{-1} was obtained from Langmuir isotherm, which was best fitted with the experimental q_e values of 1,320.9 mg g^{-1} (Table S3). The above results confirmed that the MB adsorption performance of ABH-1:3 was dramatically enhanced compared with other reported adsorbents. For comparative study, the Q_{max} values of ABH-1:3 and other similar adsorbents were collected and shown in Table 1 [22,24,37,41-44].

4. Adsorption Kinetics

For evaluating the adsorption performance of an adsorbent, the search for optimum contact time of the adsorption reaction is necessary. The adsorption kinetics experiments of four different adsorbents (ABH-1:0, ABH-1:1, ABH-1:2 and ABH-1:3) were conducted with the initial MB concentration of 700 mg L^{-1} at 298 K with different contact time (Fig. 6(a)). As depicted in Fig. 6(a), the adsorption rate and capacity of MB on four samples increased with increasing contact time and all reached equilibrium after 12 h.

Comparing ABH-1:3 with the other three adsorbents, the adsorption rate of ABH-1:3 was faster than other sorbents within the first 10 min, which could attain 94%, due to the availability of abundant adsorption sites on the surface. The adsorption equilibrium of ABH-1:3 was reached within 50 min, which was 28.8-times higher than that of ABH-1:0 (1,440 min). It could be attributed to the repulsive forces of the internal particle diffusion in the solid and bulk phases of ABH-1:0, indicating it takes much time to reach equilibrium. The rapid adsorption indicates the high removal efficiency of porous ABH-1:3, which is essential in practical application. In addition, the maximum equilibrium adsorption capacity of ABH-1:3 was 1,320.9 mg g^{-1}.

In this study, adsorption kinetics was investigated by fitting the kinetic data with several kinetics models, such as pseudo-first-order, pseudo-second-order, and intraparticle diffusion kinetic model. The rate equations can be expressed as follows [42,45]:

$$q_t = q_e(1 - e^{-k_1 t}) \tag{10}$$

$$q_t = \frac{k_2 q_e^2 t}{1 + t k_2 q_e} \tag{11}$$

$$q_t = k_i t^{1/2} + C_i \tag{12}$$

where q_t (mg g^{-1}) and q_e (mg g^{-1}) are the sorption amount at time t and equilibrium condition, respectively; t (min) is the contact time. k_1 (min^{-1}), k_2 (g mg^{-1} min^{-1}) and k_i (mg g^{-1} $min^{1/2}$) are the rate constants of the pseudo-first order, the pseudo-second order, and intraparticle diffusion, respectively; C_i (mg g^{-1}) is a constant that characterizes the thickness of the boundary layer.

The kinetics parameters obtained from the plot of experimental data are all presented in Table S4. The linear fitting lines of three

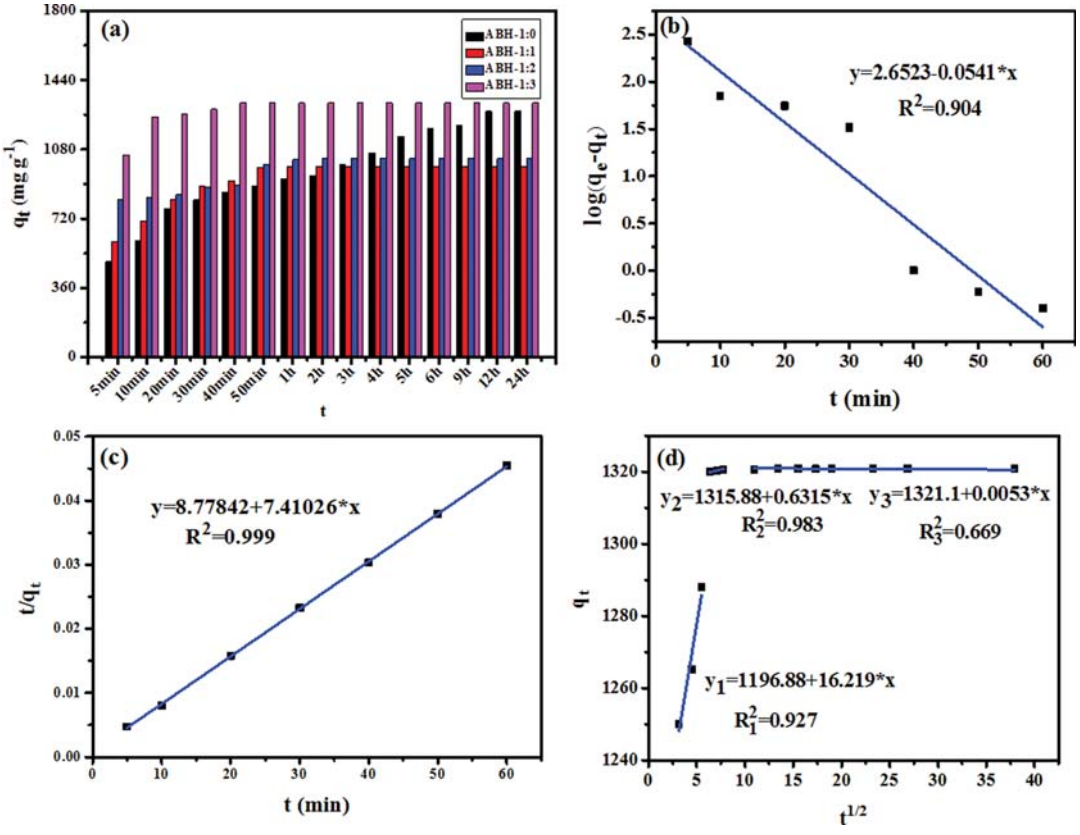

Fig. 6. The effect of contact time (a) on the adsorption of MB on different adsorbents; pseudo-first order model (b), pseudo-second order model (c) and intra-particle diffusion model (d) of MB adsorption on ABH-1:3 (adsorbent dose, 10 mg; initial MB concentration, 700 mg L^{-1}; volume, 20 mL and temperature, 298±2 K).

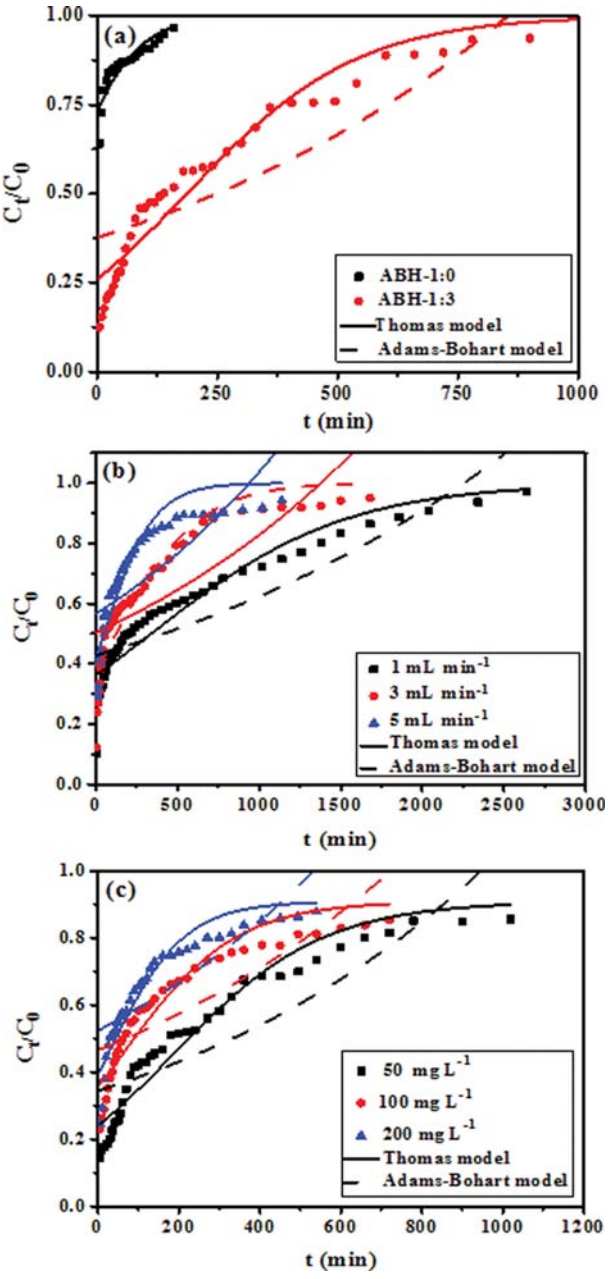

Fig. 7. Breakthrough curves (Thomas and Adams-Bohart models) of (a) ABH-1:0 and ABH-1:3 (bed height, 10 cm; initial concentration, 50 mg L^{-1}; flow rate, 5 mL min^{-1}); (b) different flow rates (bed height, 10 cm; initial MB concentration, 100 mg L^{-1}) and (c) different initial MB concentrations (bed height, 10 cm; flow rate, 5 mL min^{-1}) of MB adsorption by ABH-1:3.

kinetic models are depicted in Fig. 6. It can be observed that the correlation coefficient (R^2=0.999) obtained from pseudo-second-order model was higher than that of other kinetics models, and the calculated equilibrium adsorption capacity q_e of pseudo-second-order model was closer to the experimental data. Therefore, the pseudo-second order kinetics model fitted the experimental data best, which indicates that chemical adsorption was the main rate controlling step in the adsorption process.

5. Fixed-bed Column Adsorption

5-1. Comparative Study between ABH-1:0 and ABH-1:3

Fig. 7(a) shows the fixed-bed adsorption breakthrough curves obtained from the adsorption of MB by both ABH-1:0 and ABH-1:3. The corresponding parameters were calculated and shown in Table 2. We found that the longer exhaustion time was reached by ABH-1:3 than ABH-1:0 for the adsorption of MB. Moreover, the volume of wastewater processed at the exhaustion points of ABH-1:0 and ABH-1:3 was 1.1 and 5.1 L, respectively. These phenomena can be explained by the fact that the ABH-1:3 has higher specific surface area compared with the ABH-1:0. The above results indicate that the adsorption performance of ABH-1:3 towards MB was much better than ABH-1:0.

5-2. Fixed-bed Column Modeling

In this work, two well-known dynamic adsorption models, Thomas and Adams-Bohart models, were utilized to describe the dynamic behavior of fixed bed columns. The Thomas model assumes that the adsorption axial dispersion is negligible in the column, and the adsorption follows second-order reversible reaction kinetics. The saturated adsorption capacity and adsorption rate constant of the adsorption column can be calculated by the Thomas model, and the expression could be written as [47]:

$$\frac{C_t}{C_0}=\frac{1}{1+\exp\left(\frac{K_T q_0 M}{Q}-K_{Th}C_0 t\right)} \tag{13}$$

While, the Adams-Bohart model assumes that the adsorption rate is directly proportional to the effective area of the adsorbent and the solute concentration of the adsorbing species, and the equilibrium adsorption is not instantaneous. This model is usually used to describe the initial stage of the breakthrough curve and can be expressed as [48]:

$$\frac{C_t}{C_0}=\exp\left(K_{AB}C_0 t-K_{AB}N_0\frac{Z}{F}\right) \tag{14}$$

where K_T (L (min mg)$^{-1}$) and K_{AB} (L (min mg)$^{-1}$) are the Thomas model constant and the Adams-Bohart kinetics constant, respectively; t (min) is the service time. C_0 (mg L^{-1}) and C_t (mg L^{-1}) are the initial concentration and the effluent concentration at time t, respectively; Q (mL min^{-1}), M (g) and q_0 (mg g^{-1}) are the flow rate, sorbent mass and adsorption capacity of the adsorbent, respectively. N_0 (mg mL^{-1}) and Z (cm) are the saturation concentration and the bed height, respectively; F (cm min^{-1}) is the linear velocity which can be calculated by dividing the flow rate by the column section area.

The parameters of Thomas and Adams-Bohart models can be

Table 2. Fixed-bed column adsorption parameters for MB using ABH-1:0 and ABH-1:3

Adsorbent	Q (mL min^{-1})	C_0 (mg L^{-1})	t_e (min)	q_{total} (mg)	q_e (mg g^{-1})	V_E (L)
ABH-1:0	5	50	220	1.467	41.905	1.100
ABH-1:3	5	50	1020	66.772	1907.759	5.126

Table 3. Parameters of Thomas and Adams-Bohart model analyzed for MB adsorption ABH-1:3 in a fixed-bed column

Parameter	Thomas model			Adams-Bohart model		
	K_T (L (min mg)$^{-1}$)	q_0 (mg g^{-1})	R^2	K_{AB} (L (min mg)$^{-1}$)	N_0 (mg L^{-1})	R^2
Adsorbent						
ABH-1:0	3.03×10^{-4}	468.04	0.7733	3.20×10^{-5}	7966.14	0.6547
ABH-1:3	1.12×10^{-4}	1336.29	0.9359	2.28×10^{-5}	42671.93	0.7297
Flow rate (mL min^{-1})						
1	1.68×10^{-5}	1002.8	0.9118	2.20×10^{-5}	44851.56	0.7639
3	3.88×10^{-5}	1079.5	0.8974	1.00×10^{-5}	82265.06	0.6403
5	6.63×10^{-5}	726.16	0.8893	6.00×10^{-6}	93601.99	0.5765
Influent concentration (mg L^{-1})						
50	1.09×10^{-4}	1330.84	0.9402	3.37×10^{-6}	43830.52	0.7361
100	7.22×10^{-5}	892.11	0.9031	4.99×10^{-6}	66441.08	0.6798
200	5.38×10^{-5}	687.61	0.9063	6.05×10^{-6}	91179.01	0.6601

obtained from the intercept and slope of the plots (Fig. 7), and the results are presented in Table 3. It was found that the experimental breakthrough curves were all very close to the Thomas model. The values of the correlation coefficients (R^2) obtained from the Thomas model were higher than those of Adams-Bohart model, indicating that the breakthrough data at all experimental conditions were well described by the Thomas model. As can be seen that the value of K_T increased with increasing the flow rate and while the maximum adsorption capacity q_0 was opposite, because the external mass resistance at the surface of ABH-1:3 decreased with the increase of flow rate. Moreover, the values of K_T and q_0 decreased as the influent concentration increased, due to the limited number of active sites and unsaturated adsorption at higher influent concentrations. Similar results as obtained in this study have been reported [48]. The saturation concentration N_0 increased with the increase of flow rate and inlet concentration, while the value of K_{AB} decreased, indicating that the external mass was dominant in the initial stage of MB sorption. The maximum adsorption capacity of adsorbent was 1,330.8 mg g^{-1} at an inlet MB concentration of 50 mg L^{-1}. According to the results, the lower initial concentration had a higher adsorption capacity of MB onto ABH-1:3 in the column.

6. Adsorption Thermodynamics

To evaluate the thermodynamic feasibility and spontaneity of MB sorption onto the biocomposites, three basic thermodynamic parameters, Gibbs free energy change (ΔG^o), entropy change (ΔS^o) and enthalpy change (ΔH^o), were calculated by the following equations:

$$\ln K_L = \frac{\Delta S}{R} - \frac{\Delta H}{RT} \quad (15)$$

$$K_L = \frac{q_e}{C_e} \quad (16)$$

$$\Delta G = \Delta H - T\Delta S \quad (17)$$

where K_L, R and T are the distribution coefficient (L g^{-1}), the ideal gas constant (8.314 J mol^{-1} K^{-1}) and the absolute temperature (K), respectively. ΔH and ΔS are calculated from the slope and intercept of the linear plot of ln K_L versus 1/T. The results are shown in Fig. S4 (Supporting materials). The ΔH, ΔS and ΔG values are listed in Table S5 (Supporting materials). The negative values of ΔG indicate that the MB adsorption processes were feasibly spontaneous under the experimental conditions. The negative ΔH value revealed the exothermic nature, which corresponded with the phenomenon those adsorption capacities of MB decreased with the increase of temperature. It indicated that higher temperature is unfavorable for adsorption. In addition, the value of ΔH (−36.35 kJ mol^{-1}) was less than 40 kJ mol^{-1}, which indicates that the adsorption of MB on ABH-1:3 can be regarded as physisorption. The positive value of ΔS revealed the improved randomness, which occurred at the solid-liquid interface during the adsorption process.

7. Desorption and Reusability

In addition, reusability and regeneration of adsorbents are very important parameters for practical applications in the removal of MB from wastewater. The regeneration of adsorbent after adsorbing MB is shown in Fig. 8. It is shown that the adsorbent still had a high MB removal efficiency of over 75% even after ten adsorption/desorption cycles using 0.1 M HCl/ethanol solutions (20 mL) as an eluent, which proved the effectiveness of regeneration and recycling of the newly fabricated porous hydrogels bead-like sorbent.

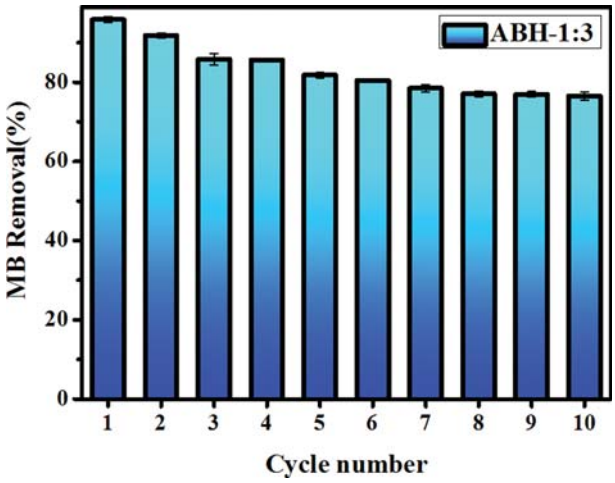

Fig. 8. The reusability of ABH-1:3 for the adsorption of MB (adsorbent dose, 10 mg; MB concentration, 700 mg L^{-1}; contact time, 1 h and temperature, 298±2 K).

CONCLUSIONS

Porous alginate-based hydrogels (porous ABH) were "greenly" prepared by facile and sustainable template-assisted method. The sorption capacities of ABH-1:3 towards MB were thoroughly compared with ABH-1:0 in batch and fixed-bed column adsorption studies. The ABH-1:3 exhibited a maximum adsorption capacity of 1,426.0 mg g^{-1} for MB by Langmuir fitting. Through the loading of nano-$CaCO_3$, the adsorption capacity and adsorption rate of adsorbent were remarkably improved. The kinetic model can be well fitted by the pseudo-second order rate equation. The thermodynamic study confirmed that the adsorption was spontaneous and exothermic. More significantly, after adsorption, ABH-1:3 could be easily regenerated for at least ten times by using 0.1 M HCl/ethanol as the eluent, and the uptake capacity of ABH-1:3 was still higher than 75% of the maximum adsorption capacity even after ten cycles. The ABH-1:3 displayed high adsorption capacity, excellent recycling stability and adsorption rate, demonstrating that it can be a promising material for the removal of MB from aqueous solution.

ACKNOWLEDGEMENTS

Financial support from the National Natural Science Foundation of China (21676039) and Innovative talents in Liaoning universities and colleges (LR2017045) is appreciated.

SUPPORTING INFORMATION

Additional information as noted in the text. This information is available via the Internet at http://www.springer.com/chemistry/journal/11814.

REFERENCES

1. K. A. G. Gusmão, L. V. A. Gurgel, T. M. S. Melo and L. F. Gil, *Dyes Pigm.*, **92**, 967 (2012).
2. M. Rafatullah, O. Sulaiman, R. Hashim and A. Ahmad, *J. Hazard. Mater.*, **177**, 70 (2010).
3. H. Métivier-Pignon, C. Faur-Brasquet and P. L. Cloirec, *Sep. Purif. Technol.*, **31**, 3 (2003).
4. H. Tu, Y. Yu, J. J. Chen, X. W. Shi, J. L. Zhou, H. B. Deng and Y. M. Du, *Polym. Chem.*, **8**, 2913 (2017).
5. D. Z. Ma, B. D. Zhu, B. Cao, J. Wang and J. W. Zhang, *Appl. Surf. Sci.*, **422**, 944 (2017).
6. J. Y. Lin, C. Y. Tang, W. Y. Ye, S. P. Sun, S. H. Hamdan, A. Volodin, C. V. Haesendonck, A. Sotto, P. Luis and B. V. Bruggena, *J. Membr. Sci.*, **493**, 690 (2015).
7. M. N. Chong, B. Jin, C. W. K. Chow and C. Saint, *Water Res.*, **44**, 2997 (2010).
8. R. D. G. Franca, A. Vieira, A. M. T. Mata, G. S. Carvalho, H. M. Pinheiro and N. D. Lourenco, *Water Res.*, **85**, 327 (2015).
9. Z. B. Wu, H. Zhong, X. Z. Yuan, H. Wang, L. L. Wang, X. H. Chen, G. M. Zeng and Y. Wu, *Water Res.*, **67**, 330 (2014).
10. E. N. Seyahmazegi, R. Mohammad-Rezaei and H. Razmi, *Chem. Eng. Res. Des.*, **109**, 824 (2016).
11. K. T. Wong, N. C. Eu, S. Ibrahim, H. Kim, Y. Yoon and M. Jang, *J. Clean. Prod.*, **115**, 337 (2016).
12. C. A. P. Almeida, N. A. Debacher, A. J. Downs, L. Cottet and C. A. D. Mello, *J. Colloid Interface Sci.*, **332**, 46 (2009).
13. K. L. Song, H. L. Xu, L. Xu, K. L. Xie and Y. Q. Yang, *Bioresour. Technol.*, **232**, 254 (2017).
14. J. L. Lv, S. R. Zhai, Y. Fan, Z. M. Lei and Q. D. An, *J. Taiwan Chem. Eng.*, **62**, 209 (2016).
15. H. Zhang, L. Chen, L. F. Li, Y. Z. Yang and X. G. Liu, *J. Porous Mater.*, **24**, 341 (2017).
16. H. U. Rehman, A. Aman, M. A. Nawaz, A. Karim, M. Ghani, A. H. Baloch and S. A. U. Qader, *Int. J. Biol. Macromol.*, **82**, 127 (2016).
17. Y. L. Zong, Y. D. Zhang, X. Y. Lin, D. Ye, D. Qiao and S. N. Zeng, *RSC Adv.*, **7**, 31352 (2017).
18. D. B. Wu, L. Zhang, L. Wang, B. H. Zhu and L. Y. Fan, *J. Chem. Technol. Biotechnol.*, **86**, 345 (2011).
19. P. Sikorski, F. Mo, G. Skjåk-Bræk and B. T. Stokke, *Biomacromolecules*, **8**, 2098 (2007).
20. Y. Zhuang, F. Yu, J. H. Chen and J. Ma, *J. Environ. Chem. Eng.*, **4**, 147 (2016).
21. N. Mohammed, N. Grishkewich, H. A. Waeijen, R. M. Berry and K. C. Tam, *Carbohydr. Polym.*, **136**, 1194 (2016).
22. A. Benhouria, M. A. Islam, H. Zaghouane-Boudiaf, M. Boutahala and B. H. Hameed, *Chem. Eng. J.*, **270**, 621 (2015).
23. A. F. Hassan, A. M. Abdel-Mohsen and M. M. G. Fouda, *Carbohydr. Polym.*, **102**, 192 (2014).
24. N. Mohammed, N. Grishkewich, R. M. Berry and K. C. Tam, *Cellulose*, **22**, 3725 (2015).
25. L. B. Sun, A. G. Li, X. D. Liu, X. Q. Liu, D. W. Feng, W. G. Lu, D. Q. Yuan and H. C. Zhou, *J. Mater. Chem. A*, **3**, 3252 (2015).
26. E. Platero, M. E. Fernandez, P. R. Bonelli and A. L. Cukierman, *J. Colloid Interface Sci.*, **491**, 1 (2017).
27. Q. Huang, M. Y. Liu, J. Zhao, J. Y. Chen, G. J. Zeng, H. Y. Huang, J. W. Tian, Y. Q. Wen, X. Y. Zhang and Y. Wei, *Appl. Surf. Sci.*, **427**, 535 (2018).
28. X. T. Liang, X. Y. Fan, R. M. Li, S. Li, S. K. Shen and D. D. Hu, *Bioresour. Technol.*, **250**, 178 (2018).
29. T. Ataei-Germi and A. Nematollahzadeh, *J. Colloid Interface Sci.*, **470**, 172 (2016).
30. D. Shan, M. J. Zhu, H. G. Xue and S. Cosnier, *Biosens. Bioelectron.*, **22**, 1612 (2007).
31. L. Li, Y. Fang, R. Vreeker, I. Appelqvist and E. Mendes, *Biomacromolecules*, **8**, 464 (2007).
32. L. N. Jin, X. S. Zhao, X. Y. Qian and M. D. Dong, *J. Colloid Interface Sci.*, **509**, 245 (2018).
33. J. de Souza Macedo, N. B. da Costa Júnior, L. E. Almeida, E. F. da SilvaVieira, A. R. Cestari, L. de Fátima Gimenez, N. L. V. Carreño and L. S. Barreto, *J. Colloid Interface Sci.*, **298**, 515 (2006).
34. J. Díaz-Terán, D. M. Nevskaia, J. L. Fierro, A. J. López-Peinado and A. Jerez, *Micropor. Mesopor. Mater.*, **60**, 173 (2003).
35. X. G. Chen and H. J. Park, *Carbohydr. Polym.*, **53**, 355 (2003).
36. P. Agulhon, V. Markova, M. Robitzer, F. Quignard and T. Mineva, *Biomacromolecules*, **13**, 1899 (2012).
37. T. Lu, T. Xiang, X. L. Huang, C. Li, W. F. Zhao, Q. Zhang and C. S. Zhao, *Carbohydr. Polym.*, **133**, 587 (2015).
38. P. Luo, B. Zhang, Y. F. Zhao, J. H. Wang, H. Q. Zhang and J. D. Liu,

Korean J. Chem. Eng., **28**, 800 (2011).
39. C. Z. Zhang, J. J. Su, H. X. Zhu, J. H. Xiong, X. L. Liu, D. X Li, Y. M. Chen and Y. H. Li, *RSC Adv.*, **7**, 34182 (2017).
40. Z. G. Zhu, P. Wu, G. J. Liu, X. F. He, B. Y. Qi, G. F. Zeng, W. Wang, Y. H. Sun and F. Y. Cui, *Chem. Eng. J.*, **313**, 957 (2017).
41. V. Rocher, A. Bee, J. M. Siaugue and V. Cabuil, *J. Hazard Mater.*, **178**, 434 (2010).
42. L. Liu, Y. Z. Wan, Y. D. Xie, R. Zhai, B. Zhang and J. D. Liu, *Chem. Eng. J.*, **187**, 210 (2012).
43. N. Belhouchat, H. Zaghouane-Boudiaf and C. Viseras, *Appl. Clay Sci.*, **135**, 9 (2017).
44. A. Salisu, M. M. Sanagi, A. A. Naim and K. J. Karim, *Der Pharma Chemica*, **7**, 237 (2015).
45. A. A. Oladipo and M. Gazi, *J. Water Process Eng.*, **2**, 43 (2014).
46. Q. Li, X. Tang, Y. Y. Sun, Y. F. Wang, Y. C. Long, J. Jiang and H. Xu, *RSC Adv.*, **5**, 25337 (2015).
47. Y. Liu, G. X. Zhong, Z. C. Liu, M. J. Meng, Y. H. Jiang, L. Ni, W. L. Guo and F. F. Liu, *RSC Adv.*, **5**, 85691 (2015).
48. K. Vijayaraghavan, J. Jegan, K. Palanivelu and M. Velan, *Sep. Purif. Technol.*, **44**, 53 (2005).

Supporting Information

Hydrogels with diffusion-facilitated porous network for improved adsorption performance

Yan-yan Pei[‡], Dong-mei Guo[‡], Qing-da An[†], Zuo-yi Xiao, Shang-ru Zhai[†], and Bin Zhai

Faculty of Light Industry and Chemical Engineering, Dalian Polytechnic University, Dalian 116034, China
(*Received 4 May 2018 • accepted 25 October 2018*)

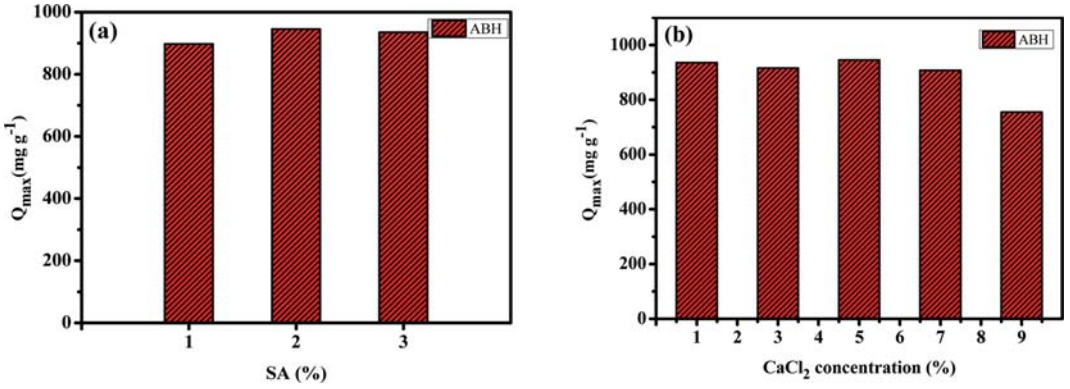

Fig. S1. Influence of SA (a) and $CaCl_2$ (b) concentrations on MB adsorption (adsorbent dose, 10 mg; initial concentration of MB, 700 mg L^{-1}; volume, 20 mL; and temperature, 298±2 K).

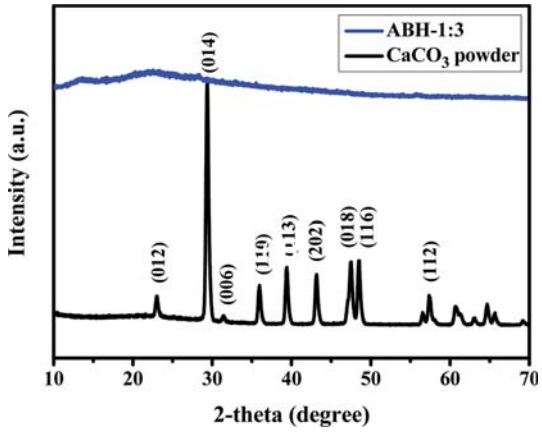

Fig. S2. XRD patterns of the $CaCO_3$ powder and ABH-1:3.

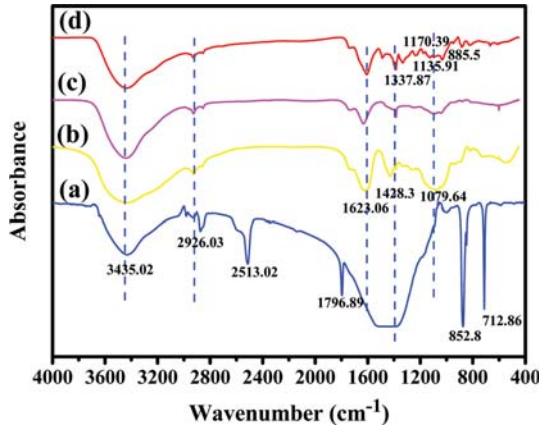

Fig. S3. FTIR spectra of the $CaCO_3$ (a), ABH-1:0 (b), ABH-1:3 before (c) and after (d) MB adsorption.

Table S1. ABH prepared with different concentration of Ca^{2+} and SA

SA (w/v)	Ca^{2+}	Q_{max} (mg g^{-1})
2%	1%	935.75
2%	3%	915.58
2%	5%	945.33
2%	7%	907.45
2%	9%	754.7
1%	5%	897.6
3%	5%	935.0

Table S2. Textural properties of the obtained ABH-1:0, ABH-1:1, ABH-1:2 and ABH-1:3

Sample	S_{BET} (m^2 g^{-1})	V_{total} (cm^3 g^{-1})	W (nm)
ABH-1:0	21.819	0.116	5.79
ABH-1:1	57.463	0.104	4.801
ABH-1:2	73.067	0.050	3.798
ABH-1:3	91.935	0.043	3.449

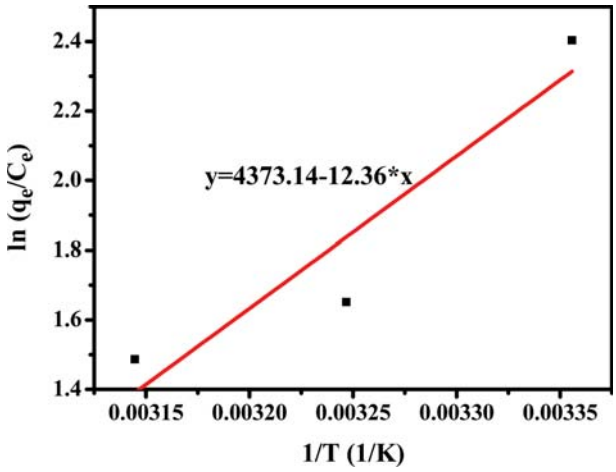

Fig. S4. The relationship between ln q_e/C_e and 1/T for MB adsorption of ABH-1:3.

Table S3. Parameters of the Langmuir, Freundlich and Temkin isotherms for adsorption of MB on ABH-1:3

Isotherm models	Parameters	Sample
		ABH-1:3
Langmuir	q_{max} (mg g^{-1})	1426.0
	K_L (L mg^{-1})	0.0284
	R^2	0.993
Freundlich	K_F (mg g^{-1})	152
	1/n	0.396
	R^2	0.912
Temkin	A (L mg^{-1})	0.378
	B (mg g^{-1})	279.49
	R^2	0.985

Table S4. Kinetic parameters of pseudo first- and second-order adsorption kinetic models and intra-particle diffusion model

Sample		Pseudo-first order			Pseudo-second order			Intra-particle diffusion					
ABH-1:3	$q_{e,exp}$	k_1	$q_{e,cal}$	R^2	k_2	$q_{e,cal}$	R^2	$k_{i,1}$	R_1^2	$k_{i,2}$	R_2^2	$k_{i,3}$	R_3^2
	1320.9	0.124	1449	0.90	0.01	1349	0.999	16.219	0.927	0.635	0.983	0.005	0.679

Table S5. Thermodynamic parameters calculated for the adsorption of dyes by the ABH-1:3

Thermodynamic parameters	Temperature	ABH-1:3
ΔH (KJ mol^{-1})		−36.35
ΔS (J mol^{-1} K^{-1})		102.76
ΔG (KJ mol^{-1})	298 K	−5.74
	308 K	−4.71
	318 K	−3.68